

Research Article

Numerical Evaluation of CFD-DEM Coupling Applied to Lost Circulation Control: Effects of Particle and Flow Inertia

Marcos V. Barbosa , Fernando C. De Lai , and Silvio L. M. Junqueira 

Federal University of Technology-Paraná—UTFPR, Postgraduate Program in Mechanical and Materials Engineering—PPGEM, Research Center for Rheology and Non-Newtonian Fluids—CERNN, 81280-340, R. Deputado Heitor Alencar Furtado, 5000-Bloco N-Ecoville, Curitiba, PR, Brazil

Correspondence should be addressed to Silvio L. M. Junqueira; silvio@utfpr.edu.br

Received 3 May 2019; Accepted 11 September 2019; Published 20 October 2019

Guest Editor: Qijun Zheng

Copyright © 2019 Marcos V. Barbosa et al. This is an open access article distributed under the Creative Commons Attribution License, which permits unrestricted use, distribution, and reproduction in any medium, provided the original work is properly cited.

In the present study, the transport and deposition of solid particles to mitigate the loss circulation of fluid through a fracture transversely placed to a vertical channel is numerically investigated. These solid particles (commonly known in the industry as lost circulation materials—LCMs) are injected into the flow during the drilling operation in the petroleum industry, in hopes to control the fluid loss. The numerical simulation of the process follows a two-stage process: the first characterizes the lost circulation flow and the second the particle injection. The numerical model comprises an Eulerian–Lagrangian approach, in which the dense discrete phase model (DDPM) is combined with the discrete element method (DEM). A parametric analysis is done by varying the vertical channel Reynolds number, the particle-to-fluid density ratio, and the particle diameter. Results are shown in terms of the particle's bed geometric characteristics, focusing on the location inside the fracture where the particles deposit, and the particle bed length, height, and time spent to fill the fracture. Also monitored are the fluid loss reduction over time and the fractured channel bottom pressure (which can be related to the fracture pressure). Results indicate that using a slow/intermediate flow velocity, associated with heavy particles with small diameters, provides the best combination for the efficient mitigation of the fluid loss process.

1. Introduction

The fundamentals of flow of fluid and solid particles, or fluid-solid two-phase flow, are of great interest because of several important engineering applications, such as sediment transport, hydrocyclones, fluidized beds, filtration processes, sedimentation, cuttings removal, and wellbore stability [1].

Singular among the existing practical problems of two-phase fluid-solid flows is the loss of drilling fluid through the porous formation during the drilling process of oil exploration. The loss occurs by the leakage of drilling fluid through pores or discontinuities (such as fractures) [2] of the rock formation in the wellbore as drilling progresses. Lost circulation events have always been a significant cause of nonproductive drilling time, increasing well construction

costs. Overall, such events could be classified as “light” loss when loss rates are below 50 bbl/h, moderate for losses that range between 50 and 150 bbl/h, and severe for losses over 150 bb/h. The industry spends millions of dollars a year to combat lost circulation and its detrimental effects, such as stuck pipe and kicks [3, 4]. Commonly related to formations with high permeability (caves and vugs), the loss of circulation is intensified in the presence of fractured zones, whose effects are notably more dramatic when the fractures are connected to a network of natural fissures [5].

Historically, materials to combat the lost circulation, so-called LCM (lost circulation material), have been used by the oil industry to minimize drilling fluid losses. Such materials are typically classified as flakes, fibers, and granulars (calcium carbonate, mica, etc.). Recent strategies list a range of applications such as graphite, cross-linked pills, high fluid

loss compression, or a blending of these materials in different concentrations [6, 7]. Because of the high cost of drilling fluids, oil companies resort to a “sealing flow” technique by adding particles of selected granulometry to the drilling fluid itself, in hopes that the particles will settle along the fracture and eventually seal the leaking path, stopping the loss of drilling fluid [4, 8–10].

The study of this sealing flow is complex and frequently difficult to perform experimentally, particularly due to limitations of available equipment (harsh flow conditions) and difficulty in performing flow visualization (opacity of the medium). Nevertheless, the alternative of performing numerical modeling and simulations of sealing flow, issue to be addressed in the present work, is not without challenges of its own. The main limitation of a numerical approach has been the large computational power necessary to resolve the flow and interactions of all the individual particles flowing along with the fluid. Notwithstanding, numerical simulations of sealing flow have recently been brought to the forefront (i.e., they became practical) due to the recent advances in the available hardware and software.

When modeling fluid-particle flow in sealing problems, the model needs to be able to address not only fluid motion itself, but also the particle-fluid and the particle-particle interactions in an efficient fashion [11]. In this respect, the combination of computational fluid dynamics (CFD) and discrete element method (DEM) is recognized as one of the most powerful combinations for the numerical study of fluid-particle interactions, especially when a four-way coupling is paramount to obtaining simulation results that are realistic and accurate.

The DEM accounts for particle motion, including collisions among the particles, by solving Newton’s second law of motion for each individual particle [12]. The method considers a soft-sphere approach in which the collisions among several particles can be easily addressed in the same time step, making it a preferable choice for dense flows whether the particles are spherical or not [13].

The capability and use of the CFD-DEM combination have been reported recently in the literature for a wide range of applications, including fluidized beds [14–19], filtration processes [20–24], hole cleaning and sediment transport in the oil and gas industry [25–28], hydrocyclones, vortex flow, and instabilities [29–31], and bed-load transport [32, 33]. Specifics of the CFD-DEM coupling have also been documented, including studies of different types of DEM coupling [34], numerical errors involved in the models [35], requirements for the coupling with distinct fluid mechanics numerical models [36–38], and the use of nonspherical particles [39].

In the present work, a CFD-DEM combination is used to simulate the transport of particles along a simplified vertical and fractured wellbore. The objective is to learn how the particles behave along the fracture and how they deposit and eventually seal a leaking path of the drilling fluid, or at least reduce its loss. Of great interest is the determination via numerical simulations of the amount of fluid being lost through the fracture considering different flow configurations, characterized by the distinct flow Reynolds number,

particle-to-fluid density ratio, and particle diameter. The outcome of such parametric exercise is a prediction of when the addition of the particles will yield the sealing of the leaking path, making the sealing flow of practical interest.

2. Problem Characterization

The drilling operation consists, in a very simplified view, of the partial removal of a substrate material in order to reach an oil and gas reservoir. The substrate is removed by the action of a drilling column which carries a drill bit at the end. Due to the friction effect against the substrate, the drill bit tends to overheat when in operation; to keep it within an acceptable working temperature range, the bit is cooled by the action of a drilling fluid, injected at the top of the drilling column. This fluid flows down the drilling column, and it returns to the surface through the annular space comprised between the column and the formation.

During drilling, the operator must observe, among other factors, the so-called operational window and the equivalent circulating density. The operational window is a combination of two pressures inside the wellbore: the pore pressure and the formation pressure. The pore pressure is defined as the pressure of fluids within the pores of a reservoir; the formation pressure is the pressure at which the formation is mechanically fractured. The equivalent circulating density (ECD) is the effective density of the circulating (drilling) fluid, taking into account the pressure drop in the annulus [40].

Observing the operational window and the ECD, the drilling process may be classified as underbalanced or overbalanced (see Figure 1). Underbalanced drilling occurs when ECD is lower than the pore pressure. Conversely, an operation is overbalanced when the ECD is higher than the pore pressure. Therefore, the lost circulation tends to become more prevalent during overbalanced drilling because of the tendency of the drilling process in this case to cause fractures in the formation. It is important to notice that the lost circulation phenomenon may be intensified in the presence of fractures already present in the formation (natural fractures) in addition to those caused by the drilling process (when ECD is higher than the formation pressure) [41, 42].

When facing lost circulation in overbalanced drilling, the operator may attempt to mitigate the losses by adding particles to the circulating fluid, as mentioned previously. Remarkably, such process is feasible during operation, especially in the cases of seepage or partial losses. This is so because the particles are transported to the fluid loss region by the drilling fluid itself, depositing, accumulating, and clogging the flow path.

In the present study, the fluid loss region is represented by a discrete fracture, which mimics a naturally occurring fracture or even induced by the drilling process [43, 44]. Figure 2 shows a 2D representation of the wellbore formation with a horizontal fracture of a typical vertical drilling operation. The figure shows a longitudinal (top) and a transversal cutting plane (bottom), the fracture aperture (e_{FR}) and its depth (z_{FR}), and also the fluid

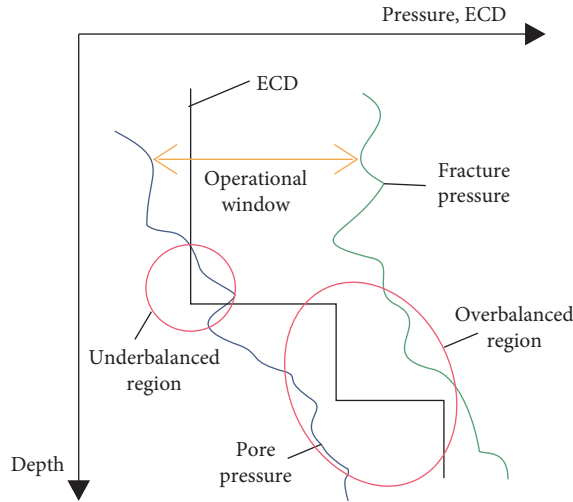


FIGURE 1: Representation of the operational window, its upper and lower limits, and ECD.

flow direction in each region of the wellbore-fracture-formation.

The geometric representation of the idealized fracture is presented in Figure 3(a). Notice that z_{FR} is significantly larger than e_{FR} , providing a symmetric inlet at the fracture region. In Figure 3(b), the red region marked as (1) is the inlet section of the fluid; (2) represents the end of the fracture; (3) symbolizes the wellbore top region; and (4) indicates the injection surface from which the particles are released. The annulus is represented by half of its hydraulic diameter (h_{CH}) which is the space between the drilling column and the wellbore wall. In relation to the fracture, whose aperture is e_{FR} , the figure also shows the upstream and the downstream lengths, l_{UP} and l_{DW} , respectively.

Another simplification adopted in this study is to consider the formation (including the fracture surfaces) impermeable. Therefore, the lost circulation analysis is limited to the fracture flow region. Consequently, the fracture filling process is analyzed without the percolation effect that typically occurs in porous reservoirs. As the porosity can be very small in these regions, the simplification effect is considered minor in respect to the flow and deposition of the particles.

To characterize the fluid loss, a two-step procedure is proposed by changing the boundary conditions applied in the problem whose goal is to observe a predetermined flow condition inside the wellbore. The flow is represented by a Reynolds number (equation (1)) defined in terms of the velocity at the wellbore inlet, $U_{\beta,CH,i}$, set at surface (1) in Figure 3(b).

$$U_{\beta,CH,i} = \frac{Re\mu_{\beta}}{\rho_{\beta}h_{CH}}, \quad (1)$$

where the subscripts β , CH, and i refer to the fluid phase, the wellbore, and the inlet region, respectively. The circulating fluid density is indicated by ρ and the viscosity by μ .

A special procedure is necessary for determining the flow boundary conditions in the domain because the fluid loss in

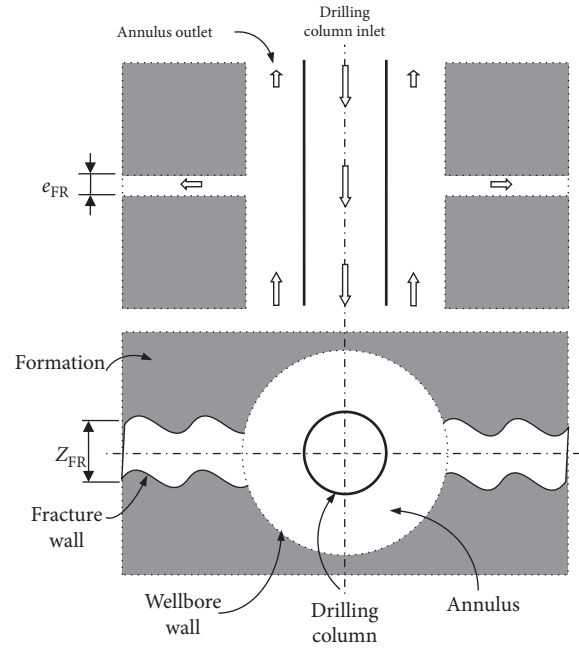


FIGURE 2: Representation of a wellbore with discrete fracture cut planes: longitudinal (top) and transversal (bottom).

a real wellbore is due to the pressure difference between the annulus and the formation, as explained earlier by the operational window, and these pressures are usually unknown. Hence, a specific amount of fluid loss is first set at the fracture outlet, q_{loss} , at surface (2), while the remainder of the circulating fluid returns to the surface, with q_{return} set at surface (3) of Figure 3(b). With all boundary conditions set, the problem is simulated until a fully developed flow condition is obtained at the annulus.

When this state is reached, the pressure at the wellbore inlet $p_{\beta,inlet}$ and the respective pressures at surfaces (2) and (3) are collected, respectively, p_{loss} and p_{return} . The second step is implemented by maintaining the velocity inlet boundary condition at surface (1) and changing the boundary conditions of surfaces (2) and (3) to the related pressures collected in the first step. Once the flow, considering the fluid loss, reaches a steady regime, the particles are released from the injection surface (4) at the same flow velocity as that of the circulating fluid to minimize any effect they might otherwise have over the fluid loss velocity field.

3. Numerical Model

The analysis of the particle transport in a fluid can be performed according to two approaches. The first one, the so-called Eulerian approach, consists of treating the particles as a continuum solid phase. This method is usually preferred when the tracking of the particles can be neglected, meaning that the particle concentration field is enough to describe the particle motion. Alternatively, in the Lagrangian approach, the particles are tracked individually throughout the domain, with their trajectories computed using Newton's second law of motion [45, 46].

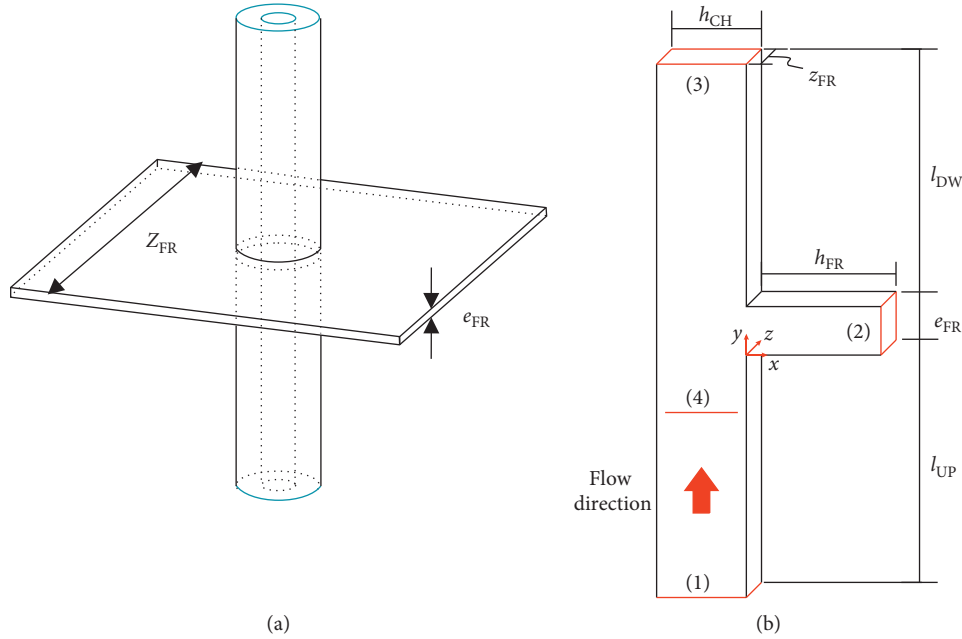


FIGURE 3: 3D domain representation and scale of the fracture plane related to the wellbore (a); fractured wellbore simplified representation (b).

In the study presented hereby, the fluid and the particles are described according to, respectively, the Eulerian and Lagrangian approaches via the dense discrete phase model (DDPM) of Ansys Fluent® software. The basics of the numerical model are presented here, with a more thorough and detailed analysis found in [47]. For the continuous phase (fluid), the mass and momentum conservation equations are described by equations (2) and (3):

$$\frac{\partial \rho_{\beta} \rho_{\beta}}{\partial t} + \nabla \cdot (\epsilon_{\beta} \rho_{\beta} \mathbf{u}_{\beta}) = 0, \quad (2)$$

$$\begin{aligned} \frac{\partial (\epsilon_{\beta} \rho_{\beta} \mathbf{u}_{\beta})}{\partial t} + \nabla \cdot (\epsilon_{\beta} \rho_{\beta} \mathbf{u}_{\beta} \mathbf{u}_{\beta}) &= -\epsilon_{\beta} \nabla \rho_{\beta} + \nabla \cdot (\epsilon_{\beta} \mu_{\beta} \nabla \cdot \mathbf{u}_{\beta}) \\ &+ \epsilon_{\beta} \rho_{\beta} \mathbf{g} + \mathbf{F}_{DPM} + \mathbf{S}_{DPM}, \end{aligned} \quad (3)$$

where t is the time, ϵ_{β} represents the continuous phase volume fraction, \mathbf{u}_{β} is the velocity vector, \mathbf{p}_{β} is the pressure gradient, \mathbf{g} refers to the gravity acceleration vector, \mathbf{F}_{DPM} refers to the coupling force between the phases, and \mathbf{S}_{DPM} is the source term due to the displacement of fluid caused by the particle entering a control volume.

Particle movement is determined using both the definition of velocity and Newton's second law of motion, given by equations (4) and (5), respectively,

$$\frac{dx_p}{dt} = \mathbf{u}_p, \quad (4)$$

$$m_p \frac{d\mathbf{u}_p}{dt} = \mathbf{F}_d + \mathbf{F}_{gb} + \mathbf{F}_{pg} + \mathbf{F}_{vm} + \mathbf{F}_{ls} + \mathbf{F}_{DEM}, \quad (5)$$

where \mathbf{x}_p and \mathbf{u}_p represent the particle position and velocity, respectively, and the particle mass is given by m_p . By

applying a Lagrangian approach to the particles, several forces can be included in the analysis of particle motion. A summary of the expressions for determining the aforementioned forces is presented in Table 1, where drag (\mathbf{F}_d), gravitational and buoyancy (\mathbf{F}_{gb}), pressure gradient (\mathbf{F}_{pg}), virtual (added) mass (\mathbf{F}_{vm}), and Saffman's lift (\mathbf{F}_{ls}) forces are considered.

Regarding equation (5), a four-way coupling accounts for the particle collisions [48]. As such, $F_{DEM} = F_n + F_t$, where the last two terms represent, respectively, the normal and the tangential components [49]. In this sense, the particles are able to collide with each other as well as with any solid surface on the numerical domain, be it a fracture or a channel surface. This means that once a particle reaches the boundary of the numerical domain, two situations may occur: if the boundary is a solid surface, the collision force is calculated using F_{DEM} ; in case of an open flow region, such as the fracture or channel outlet (surfaces 2 and 3 in Figure 1), the particle will simply exit (be eliminated from) the domain, as it happens in practical situations.

While the drag coefficient C_D is obtained from Morsi and Alexander's [50] correlation, Saffman's constant C_{ls} is calculated using Li and Ahmadi's [51] model, being the virtual mass coefficient obtained from [52].

The tangential component of the collision force is usually obtained from Coulomb's law in which μ_a is the friction coefficient and ζ_{12} represents the tangential direction. For the proposed problem, the tangential force is neglected.

The normal force is evaluated by a spring-dashpot model [53] by means of several numerical parameters. In the spring part of the model, the overlap δ is calculated with two collision partners according to their position \mathbf{x} related to their radius $\delta = |\mathbf{x}_2 - \mathbf{x}_1| - (r_1 + r_2)$. The particle stiffness constant is a numerical parameter calculated by $k = \pi |\mathbf{u}_{12}|^2 d_p \rho_p / 3 \sigma_d^2$, where σ_d represents the fraction of the

TABLE 1: Forces considered in the numerical model.

Force	Equation
Gravitational and buoyancy	$\mathbf{F}_{gb} = m_p((\rho_p - \rho_\beta)/\rho_p)g$
Drag	$\mathbf{F}_d = (3/4)(m_p\mu_\beta/\rho_p d_p^2)C_D Re_p(\mathbf{u}_\beta - \mathbf{u}_p)$
Saffman lift	$\mathbf{F}_{ls} = C_{ls}m_p(\rho_\beta/\rho_p)(\nabla \times \mathbf{u}_\beta) \times (\mathbf{u}_\beta - \mathbf{u}_p)$
Virtual mass	$\mathbf{F}_{vm} = C_{vm}m_p(\rho_\beta/\rho_p)(D/Dt)(\mathbf{u}_\beta - \mathbf{u}_p)$
Pressure gradient	$\mathbf{F}_{pg} = m_p(\rho_\beta/\rho_p)(\mathbf{u}_\beta \nabla \cdot \mathbf{u}_\beta)$
Collision	
Normal	$\mathbf{F}_n = [k\delta + \gamma(\mathbf{u}_{12} \cdot \lambda_{12})]\lambda_{12}$
Tangential	$\mathbf{F}_t = -\mu_a \mathbf{F}_n \zeta_{12}$

particle diameter that is allowed to overlap with the collision partner and \mathbf{u}_{12} is the relative velocity between the collision partners; λ_{12} indicates the normal direction of collision.

Similarly, the dashpot part modeling employs the damping coefficient γ [54], calculated from the reduced mass $m_{12} = 2m_1m_2/(m_1 + m_2)$, the coefficient of restitution (η), and from the collision time (t_{col}) as follows: $\gamma = -2m_{12}\ln(\eta)/t_{col}$.

For the simulations presented here, an extensive sensitivity analysis was performed to ensure the correct characterization of fluid motion as well as particle transport and collision. The main numerical parameters applied on the model are summarized as follows: fluid time step $\Delta t_\beta = 2 \cdot 10^{-2}$ s, particle time step $\Delta t_p = 2 \cdot 10^{-4}$ s, and particle's stiffness constant $k = 2.0$ N/m. Also, the coefficient of restitution $\eta = 0.9$ is applied for both particle-particle and particle-wall collisions. Other numerical details of the DDPM model, such as pressure-velocity coupling, pressure correction, spatial discretization, and transient formulation, are detailed in [47].

4. Results and Discussion

4.1. Verification of DDPM-DEM Capability. In order to evaluate the capability of the model to accurately predict the interaction between the solid and fluid phases, as well as to correctly determine the collision forces amongst the particles, two verification tests were carried out: the settling velocity of a single particle released in a fluid and the bouncing motion of a single particle against a static solid surface.

The settling velocity problem consists of abandoning a single sphere from a resting position inside a container of fluid and measuring its velocity up to a constant value named terminal or settling velocity. The collision problem consists, at first, of the same settling velocity problem, except that this time, the particle will collide with a static wall and bounce on it until the particle achieves a zero-velocity condition. Interacting problems of one, two, or four particles are often applied in the literature to evaluate the capacity of numerical models [55–60].

The settling velocity of a single spherical particle, presented in Figure 4(a), was simulated and compared with the numerical and experimental results of [61]. The results correspond to a particle density and diameter of

$\rho_p = 7710$ kg/m³ and $D_p = 0.8$ mm, respectively, settling in water ($\rho_\beta = 998.2$ kg/m³ and $\mu_\beta = 1.003 \cdot 10^{-3}$ Pa·s).

The results presented in Figure 4(a) show a good agreement with both the numerical model and the experimental results presented by Mordant and Pinton [61], even at the final stages of the settling process. For the settling velocity, the relative difference is less than 1%, 0.316 m/s for the experimental results and 0.313 m/s for the numerical simulation. Thus, one can conclude that the DDPM model is indeed able to calculate the interaction forces between the fluid and a particle with the inclusion of the selected forces shown at Table 1.

As the particle deposition process occurs within the fracture, particle collisions become more important. Consequently, in order to ascertain the capability of the DDPM-DEM models, outcomes from the bouncing motion of a spherical particle are compared with the experimental results from [62], as depicted in Figure 4(b). In this case, a particle with $D_p = 0.8$ mm and $\rho_p = 7800$ kg/m³ is moving in a fluid composed of a water-glycerin mixture (73.7% water in volume) with properties $\rho_\beta = 935$ kg/m³ and $\mu_\beta = 10^{-2}$ Pa·s. Prior to the first collision, the particle attains a settling velocity of roughly 0.6 m/s.

Observe the DEM model is capable to represent the wall-particle interactions, since after the first collision only a slightly lower value of the maximum velocity is observed. When the second collision happens, a time shift in the numerical simulation of roughly 0.1 s is noticed, which persists for the remaining collisions, causing a delay in the time demanded to cease the particle motion. However, it is important to notice that the speeds at each collision as well as the number of collisions were predicted correctly by the simulations.

As the particles are mostly carried in the horizontal direction of the fluid motion that occurs inside the fracture instead of being exclusively moved in the vertical direction, less interest is dedicated to the repetitive collision of a particle against a wall. Therefore, the first collision that occurs when the particle reaches the surface of the fracture demands special attention. From the analysis presented in this section, it is possible to assure that the DDPM-DEM model is indeed a good approach for the problem investigated here.

4.2. Filling a Horizontal Fracture. In the simulations to be presented, the fluid loss occurring at the end of the fracture was set as $q_{loss} = 10\%$ of the total mass flow rate. As the lost circulation phenomenon is established, the particles are released in the numerical domain from an injection surface as shown in Figure 5, with the maximum velocity attained from the fluid flow velocity profile. As the momentum exchange from particle to fluid along time occurs, the particles tend to assume the velocity of the fluid nearby. As a consequence, at a steady state, a parabolic velocity profile is verified (the color of the particle is associated to its velocity—red means faster particles). At each time step, a total of 30 particles are injected. For instance, considering

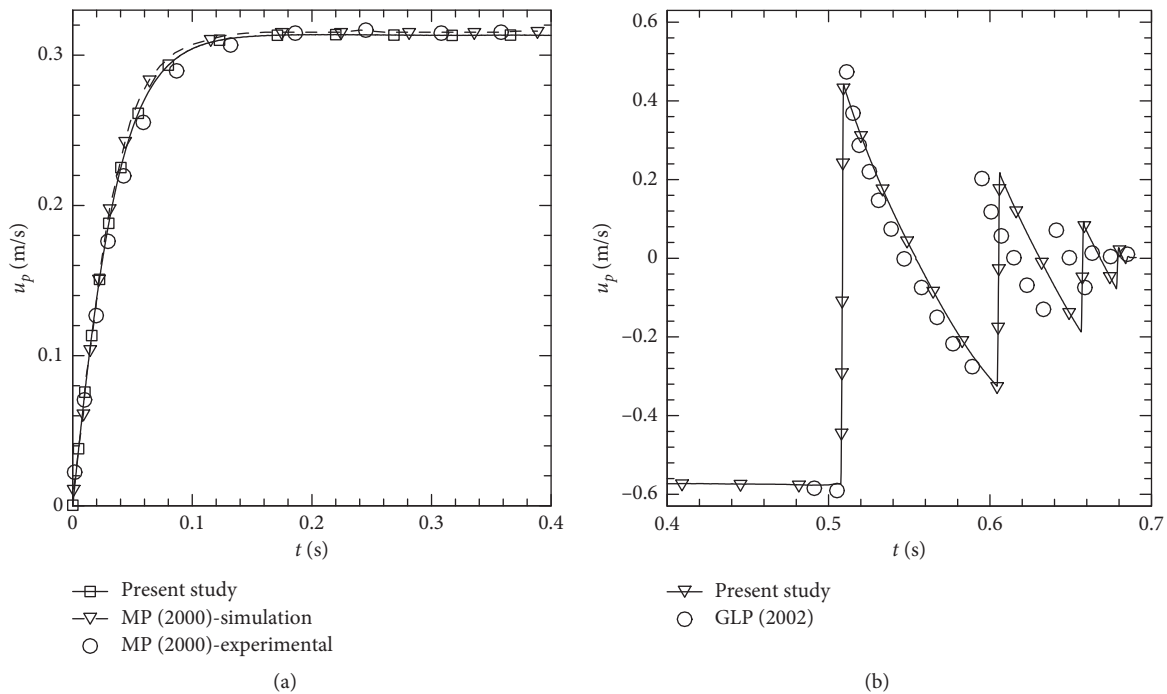


FIGURE 4: Comparison between the data from [61] (MP) (a) and [62] (GLP) (b).

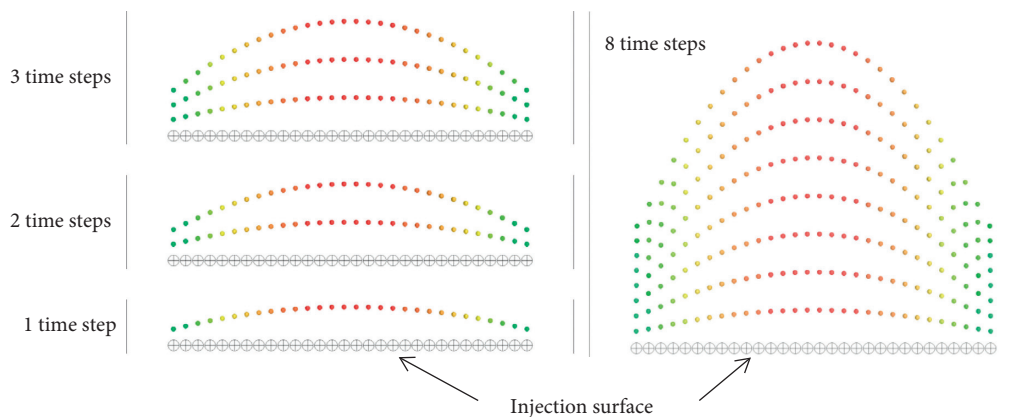


FIGURE 5: Particle injection process for several time steps.

175 seconds of injection, for a time step of $2 \cdot 10^{-2}$ seconds, 262,500 particles will be injected into the domain.

Before choosing the particle time step size, one must be certain that no particle will be released inside each other so that the overlap parameter δ is not incorrectly calculated. This is guaranteed by associating the particle velocity with the fluid time step size in a manner that the distance covered by the particle is sufficiently larger than the particle diameter. By observing this simple procedure, an incorrect particle injection can be avoided.

It is also important to understand that not all particles will enter the fracture and contribute to the filling process. In fact, depending on the particles' properties, fluid, and flow conditions, only 2 to 5% of all injected particles will ever get into the fracture. Also, as the fluid loss is reduced throughout the process, fewer particles will enter the fracture. This situation is presented in Figure 6.

The channel geometric characteristic presents an upstream length of $l_{UP} = 1.8$ m, a downstream length of $l_{DW} = 0.225$ m, and a width of $h_{CH} = 0.045$ m. The fracture was considered as impermeable with $h_{FR} = 0.720$ m in length and width $e_{FR} = 0.01$ m. The fluid considered in the simulations was a water-glycerin mixture with $\rho_{\beta} = 1187.6$ kg/m³ and $\mu_{\beta} = 27.973 \cdot 10^{-3}$ Pa·s.

The flow Reynolds number, written in terms of fluid's mean velocity ($U_{\beta,CH,i}$), equation (1), set at the channel inlet, controls the flow rate. The particle-to-fluid density ratio (ρ_P/β) and the particle diameter (D_P) are also the main parameters of the present study.

A numerical grid test, where the fluid loss stabilization was taken as the main parameter to determine mesh independence, showed that for a relative difference of 1%, no significant changes on the flow conditions and on the particle transport/deposition rate were observed.

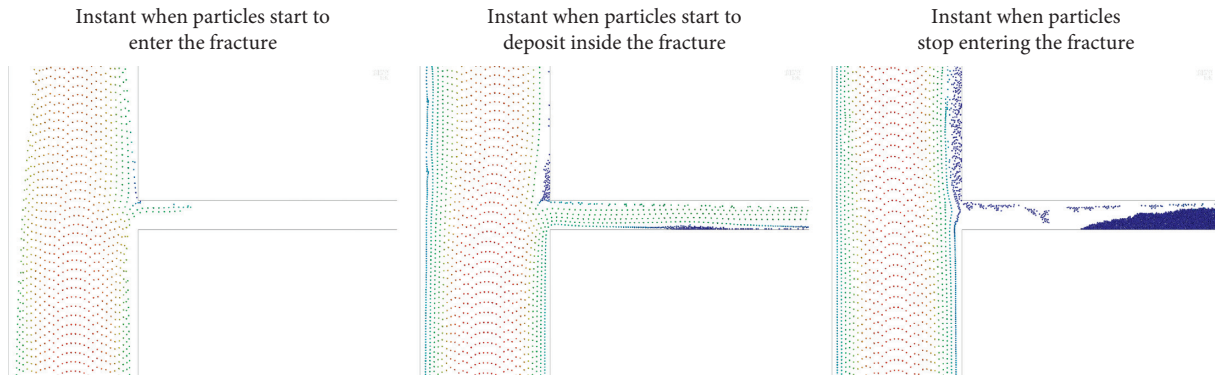


FIGURE 6: Fracture inlet region for several instants showing the variation on the amount of particle entering the fracture.

Additionally, a grid refinement, to ensure a suitable wall effect evaluation, was applied specifically for each configuration. Thus, a channel with 18000, 20000, and 22000 control volumes and respective Reynolds numbers of 250, 500, and 750 were considered. In Figure 7, a mesh detail at the fracture inlet region is shown.

Initially, the influence of the Reynolds number over the particle bed formation as well as the fluid loss through the fracture is investigated. The simulations were accomplished for three configurations, namely, $Re = 250, 500,$ and 750 , corresponding to a channel inlet velocity of $U_{\beta,CH,i} = 0.131, 0.262,$ and 0.393 m/s, respectively. For each flow time step, 1500 particles ($\rho_{p/\beta} = 2.25$ and $D_p = 0.5$ mm) are injected into the domain from the particle injection surface. Figure 8 shows the particle bed formed inside the fracture at the moment the particles cease to enter the fracture, Δt_{fill} .

One can notice a strong influence of the Reynolds number especially in the particle bed position ($h_{bed,i}$), measured as the distance from the fracture inlet to the beginning of the particle bed. Clearly, the bed position is influenced by the flow quantity of movement, which in turn also impacts the particle bed extension (h_{bed}). As expected, for low Re , the particles start to deposit closer to the fracture entrance, forming a more compact bed, which also leads to an increase in the particle bed height, represented here in terms of the fracture vertical filling percentage ($e_{\%,FR}$), as presented in Table 2.

As related to Re , the flow velocity will be different for all three conditions, even if the initial percentage of fluid loss ($q_{loss} = 10\%$) is the same for all the cases simulated. Thus, a low Re indicates a low fluid velocity in the fracture, and the reverse is also true. In this way, the flow presents more or less momentum to carry particles along the fracture as the Reynolds number is, respectively, higher or lower. Consequently, the smaller the Re is, the closer to the fracture entrance (reduction on $h_{bed,i}$) and also more compact is the particle bed, implying in a shorter length (h_{bed}) and in a larger height ($e_{\%,FR}$).

Given the flow inability to maintain particles suspended for a long period of time, it is possible to see in Table 2 that the time required to the particle deposition process (Δt_{fill}) is smaller for lower Reynolds number. Hence, to reduce the fluid loss in an impermeable fracture, the flow rate has to be

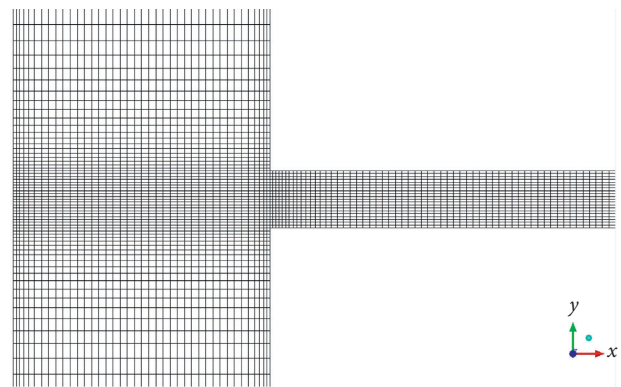


FIGURE 7: Mesh display for the fracture inlet region for $Re = 500$.

reduced to provide a faster particle deposition in the fracture.

Assuming that the understanding on how the particle injection process acts on the fluid loss through the fracture is paramount for the present study, the influence of $Q_{loss} = (q_{loss,t}/q_{loss}) \times 100\%$, defined as the ratio between the fluid lost along the particle injection ($q_{loss,t}$) and the initial fluid loss (q_{loss}), is investigated for different Re . Therefore, as shown in Figure 9(a), for a fluid loss of 100%, as the particle deposition process takes place, a reduction in the fluid escaping through the fracture is expected.

Another monitor, defined as $P_{inlet} = (p_{inlet,t}/p_{\beta,inlet}) \times 100\%$, has been configured at the inlet of the main channel, with the aim to mimic the downhole pressure. In such a monitor, presented in Figure 9(b), $p_{inlet,t}$ and $p_{\beta,inlet}$ are, respectively, the pressure at the fracture entrance along the particle injection and the initial pressure.

Figure 9(a) shows that the fluid loss is reduced to roughly 42% of the original loss for both $Re = 500$ and 750 . However, the time spent in the particle deposition process (which is indicated when the fluid loss reaches a plateau) is much higher for $Re = 750$, as described previously. By reducing the Reynolds number to 250 and consequently the flow strength, the fluid loss reaches 38%, indicating a reduction of 62% of the original fluid loss.

The downside of choosing a lower velocity for the fluid is a dramatic increase in the pressure measured at the channel inlet, as can be observed in Figure 9(b). The particles injected

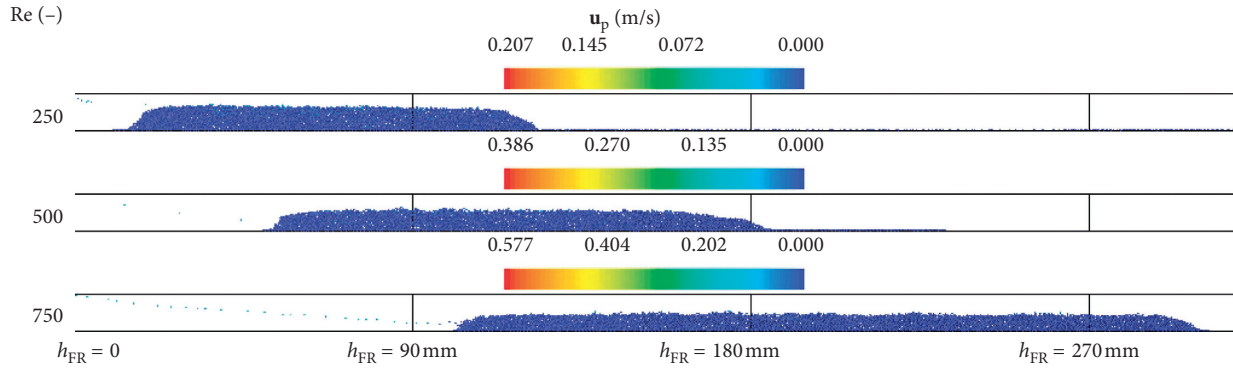


FIGURE 8: Particle bed formed inside the fracture at Δt_{fill} for Reynolds number (Re) variations ($\rho_p/\beta = 2.50$; $D_p = 0.5$ mm).

TABLE 2: Particle bed geometric characteristics in terms of Reynolds number.

$Re (-)$	$h_{bed,i}$ (mm)	h_{bed} (mm)	$e_{\%,FR}$ (%)	Δt_{fill} (s)
250	15	108	64	76
500	64	131	54	82
750	102	196	45	136

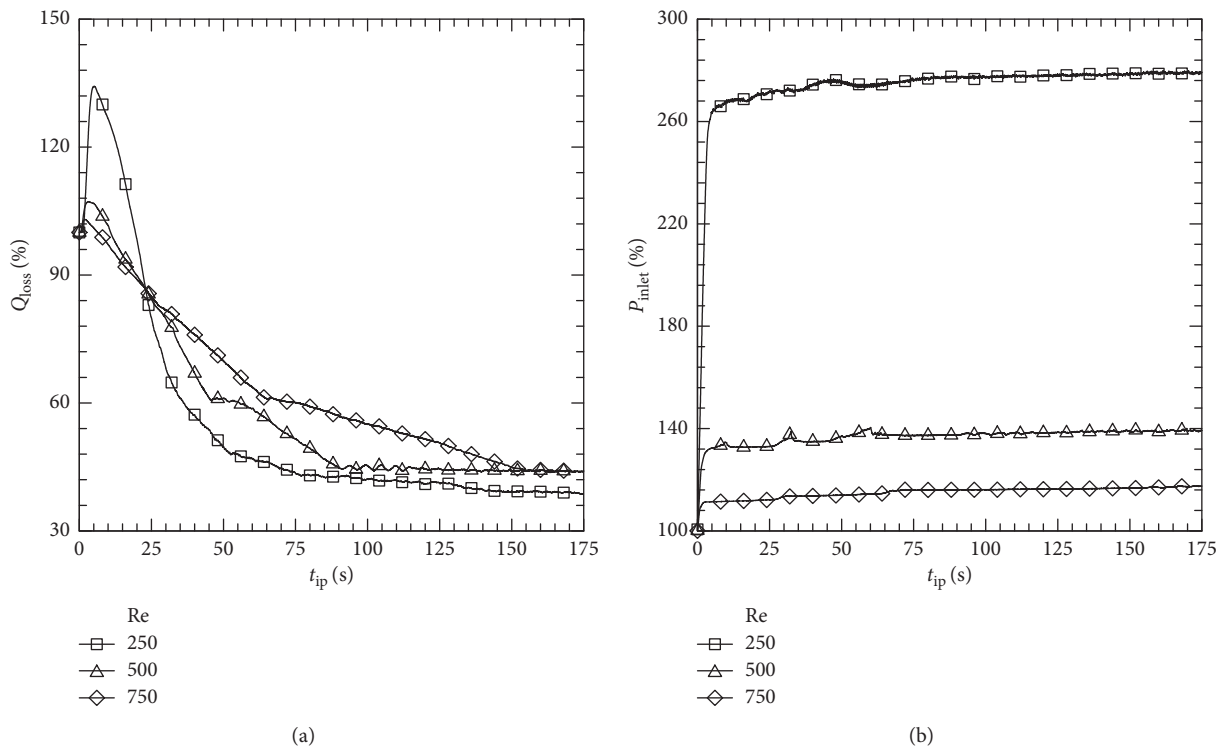


FIGURE 9: Monitoring for the fluid loss (Q_{loss}) by the fracture (a) and dimensionless pressure (P_{inlet}) at the bottom of the fractured channel (b) for Reynolds number variations ($\rho_p/\beta = 2.50$; $D_p = 0.5$ mm).

at the channel contribute to the increase in pressure due to differences in the particle-to-fluid density ratio. For lower velocities, more particles are expected to accumulate on the main (vertical) channel, which causes a prompt increase of P_{inlet} for $Re = 250$. As the particles move more rapidly throughout the domain, the increase in the pressure is less prominent.

In the second set of simulations, the influence of the particle-to-fluid density ratio (ρ_p/β) is investigated. For this, the case $Re = 500$ is set as the reference flow configuration and all the particles have diameter $D_p = 0.5$ mm. The main objective is to observe the effect of changes in the particle density over the fracture filling process. Further on, the effect of changes in the particle diameter will be presented

as well. The final condition for the particles to be packed inside the fracture is presented in Figure 10. Information on size, extension, and position of each bed is presented in Table 3.

Whilst changes in Reynolds number influence the flow strength, modifications in the particle density alter the particle quantity of movement. Consequently, the flow has more difficulty to carry heavier particles. As shown in Figure 10, the lighter the particles, the greater the h_{bed} values (see the $\rho_{p/\beta} = 1.50$ case in Table 3). On the contrary, as the particles get heavier (case $\rho_{p/\beta} = 2.50$), the fluid does not have enough momentum to carry them away. With that, a tendency of the particles to accumulate near the entrance is observed, and a more compact bed is formed.

The observations concerning the influence of the particle mass shown in Figure 10 are also related to the particle bed length, which gets larger for lighter particles. For the $\rho_{p/\beta}$ values analyzed, it seems there is a stabilization process regarding the particle bed length because no significant difference was observed between cases $\rho_{p/\beta} = 2.25$ and $\rho_{p/\beta} = 2.50$, except for a shift on the particle bed initial position $h_{\text{bed},i}$, which is related to particle quantity of movement.

Regarding the fluid loss reduction, shown in Figure 11(a), which is the main objective of this study, a slight difference when using heavier particles is noticed, since the final reduction of loss circulation ranges from 39% ($\rho_{p/\beta} = 1.50$) to 47% ($\rho_{p/\beta} = 2.50$). The use of heavier particles provides a significant reduction of the time required to fill the fracture. Nevertheless, they are not as effective as using the lighter particles to reduce the loss of fluid. Notice that the difference on the fluid loss reduction for $\rho_{p/\beta} = 1.50$ and $\rho_{p/\beta} = 2.50$ is only of 4%, while the time for the filling process is cut by 50%.

Concerning the pressure monitor at the fractured channel inlet, presented in Figure 11(b), the use of heavier particles has the drawback of increasing the pressure in this region by roughly 60%. Different from the change in fluid velocity, here the increase in pressure between the limit cases, i.e., $\rho_{p/\beta} = 1.50$ and $\rho_{p/\beta} = 2.50$, is only about 31%. Such behavior indicates that a technician, for instance, is better off choosing heavier particles for the filling process, since in this case, the pressure does not represent any significant restriction for the operation with respect to the particle density.

Finally, an alternative analysis of the particle inertia by considering different particle diameters ($D_p = 0.4, 0.5,$ and 0.6 mm) is presented in Figure 12. As pointed out earlier, the Reynolds number is fixed as 500 while the particle-to-fluid density ratio is kept as $\rho_{p/\beta} = 2.50$. Again, due to the same flow conditions, it is possible to see that the increase of particle mass due to the increase in its diameter is responsible for changing the fixed bed position along the fracture: as particle gets heavier the fluid flow gets less capable of transporting them.

Results from Figure 12 show that the particle bed length increases with the particle diameter. From the geometric characteristics of each bed, presented in Table 4, one can

notice that there is an apparent stability on the fracture filling time when $D_p = 0.5$ and 0.6 mm.

As occurred in the particle-to-fluid density ratio analysis, it is possible to see from Figure 13(a) that particles with less quantity of movement (lighter due to a smaller diameter) have the ability to more effectively reduce the fluid loss. In the case presented here, this is also related to the porosity of the bed. As a matter of fact, a more cohesive and less porous bed is formed when the particles are smaller, which in turn helps to reduce the fluid loss.

Still, the increase in P_{inlet} in Figure 13(b) is directly linked to the particle mass variation, as the flow characteristics remain the same for the three simulations. Therefore, the higher the particle mass, the higher P_{inlet} . The relative difference of 32% in P_{inlet} for the limit cases ($D_p = 0.4$ and 0.6 mm) may not be as significant for the drilling operation. Otherwise, when a comparison between $D_p = 0.5$ and 0.6 mm cases is drawn, the former presents not only a better fluid loss reduction (roughly 54%) but also a lower increase in P_{inlet} and a similar Δt_{fill} , suggesting that it would be wiser to employ particles with $D_p = 0.5$ mm.

5. Final Remarks

In this work, the reduction of the lost circulation in a horizontal fracture branching from a vertical channel emulating a fractured oil well was investigated. A numerical modeling accounting for the transport and deposition of solid particles inside the fracture was proposed. Numerical results obtained using the coupling of DDPM-DEM models proved to be a good alternative, not only to represent the two-phase flow but also to characterize the particle bed length, height, and position. This study provided a better understanding of using particles to seal a fracture, especially concerning to the oil and gas industry.

Several observations can be pointed out from the results. When injecting a fixed type of particles, an increase in the flow velocity usually increases the time spent on the filling process because the particles tend to be carried by the flow in the fracture region for longer distances. This is reflected in the particle bed formation, whose length is inversely proportional to its height. Increasing the particle-to-fluid density ratio, the particles get heavier; therefore, they tend to accumulate closer to the fracture inlet. The same behavior is verified when the particle diameter is increased: the particles also accumulate closer to the inlet region of the fracture. In both cases, the time spent to fill the fracture is reduced. Clearly, this is related to the weight of the particle since density and diameter are directly linked to particle mass.

On the contrary, particle density and diameter affect bed length and height in an opposite manner: while the particle bed length is reduced as the particle density is increased, the reverse is true for the particle diameter. This happens due to the increase in the particle mass at the annulus, providing a higher pressure and resulting in a longer particle bed.

Remarkably, the effects presented here are competitive and one can choose to increase particle inertia by

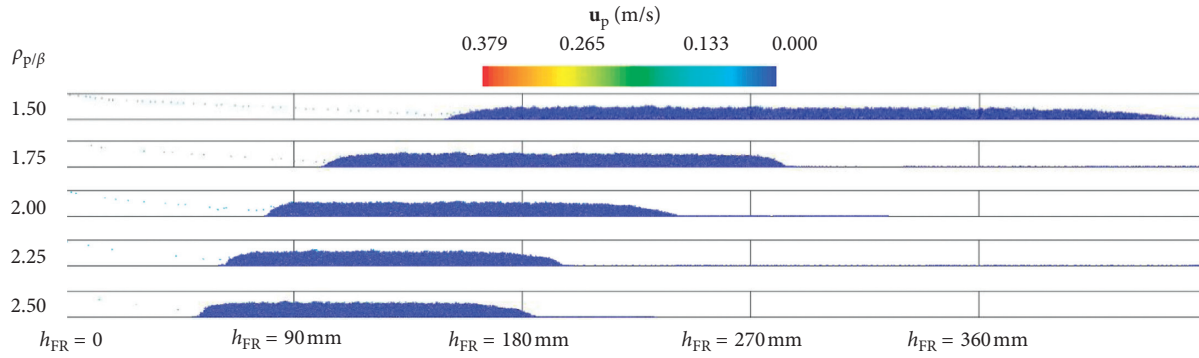


FIGURE 10: Particle bed formed inside the fracture at Δt_{fill} for particle-to-fluid density ratio (ρ_p/β) variations ($Re = 500$; $D_p = 0.5$ mm).

TABLE 3: Particle bed geometric characteristics in terms of the particle-to-fluid density ratio.

ρ_p/β	$h_{bed,i}$ (mm)	h_{bed} (mm)	$e_{\%,FR}$ (%)	Δt_{fill} (s)
1.50	150	284	43	147
1.75	101	183	50	111
2.00	79	161	52	94
2.25	64	131	54	82
2.50	53	131	57	77

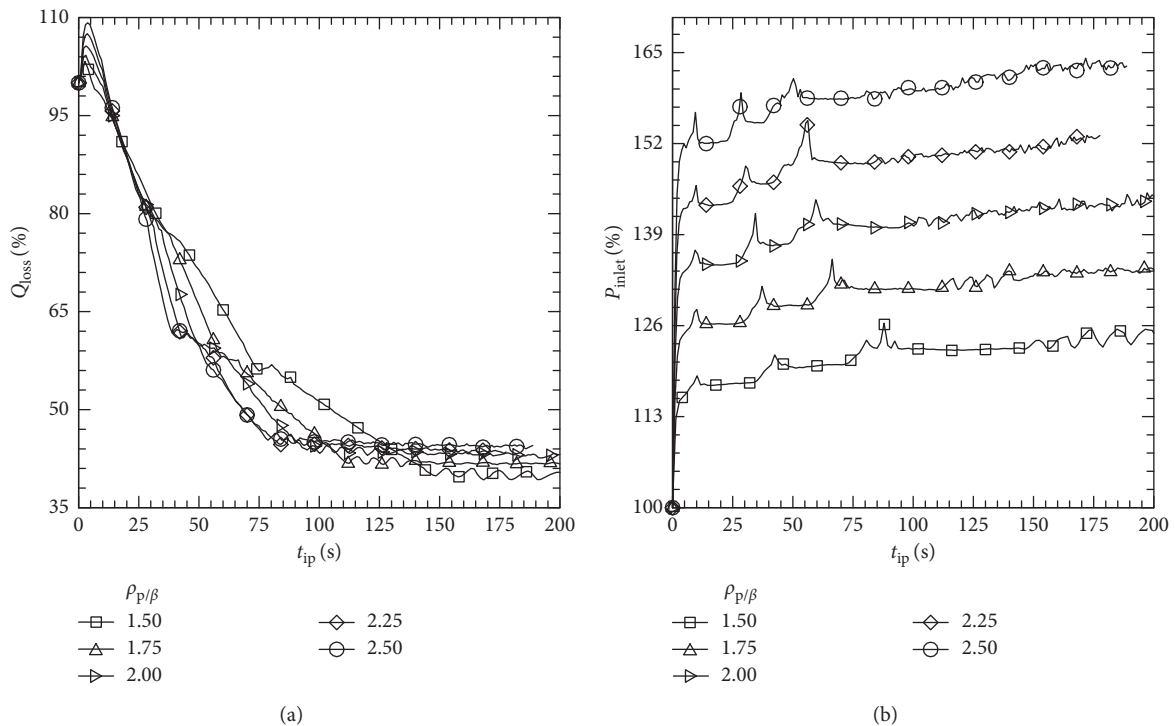


FIGURE 11: Monitoring for the fluid loss (Q_{loss}) by the fracture (a) and dimensionless pressure P_{inlet} at the fractured channel inlet (b) for particle-to-fluid density ratio variations ($Re = 500$; $D_p = 0.5$ mm).

increasing its density or diameter. Also, the same effect may be achieved by decreasing flow velocity, for instance. Bearing in mind the operational window, the operator may alter one or more parameters to achieve a specific

effect which can be represented by reducing the lost circulation to acceptable levels in the least amount of time or, if possible, curtail all losses without taking time into account.

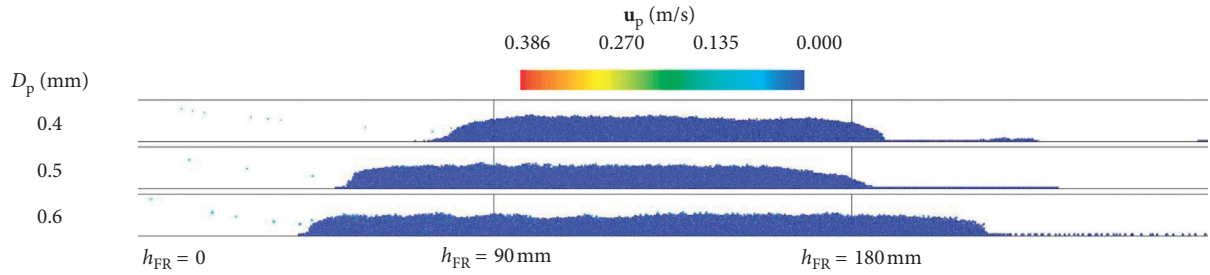


FIGURE 12: Particle bed formed inside the fracture at Δt_{fill} for particle diameter (D_p) variations ($Re = 500$; $\rho_{p/\beta} = 2.50$).

TABLE 4: Particle bed geometric characteristics as a function of the particle diameter D_p .

D_p (mm)	$h_{bed,i}$ (mm)	h_{bed} (mm)	$e_{\%,FR}$ (%)	Δt_{fill} (s)
0.4	77	111	59	111
0.5	53	131	57	77
0.6	44	169	48	77

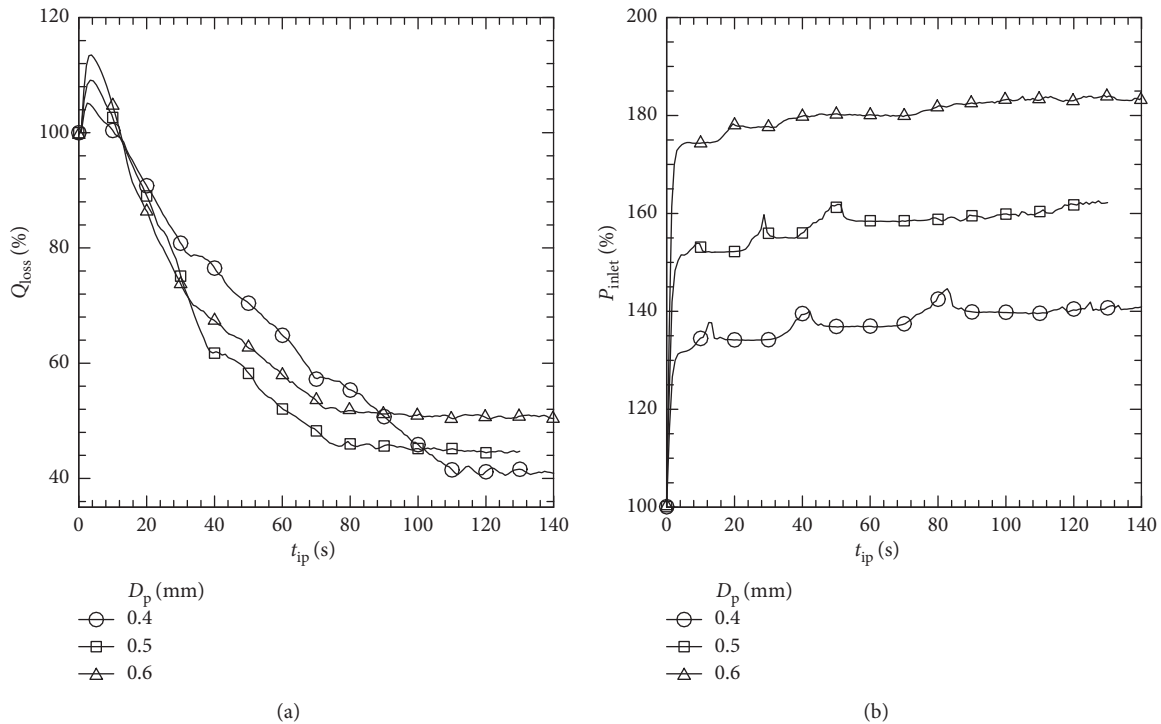


FIGURE 13: Monitoring for the fluid loss (Q_{loss}) by the fracture (a) and dimensionless pressure (P_{inlet}) at the fractured channel inlet (b) for particle diameter variations ($Re = 500$; $\rho_{p/\beta} = 2.50$).

The present study represents a development of a robust and complete methodology that can help Petrobras to optimize its drilling operations in severe loss of circulation scenarios.

Data Availability

The data used to support the findings of this study are included within the article.

Conflicts of Interest

The authors declare that they have no conflicts of interest.

Acknowledgments

The authors would like to express their gratitude to the National Council for Scientific and Technological

Development (CNPq) and Petrobras (which also provided technical assistance) for the financial support and to Professor José L. Lage from Southern Methodist University for his contribution and pertinent discussions in the development and conclusion of this work.

References

- [1] H. P. Zhu, Z. Y. Zhou, R. Y. Yang, and a. B. Yu, "Discrete particle simulation of particulate systems: a review of major applications and findings," *Chemical Engineering Science*, vol. 63, no. 23, pp. 5728–5770, 2008.
- [2] N. Morita, A. D. Black, and G.-F. Guh, "Theory of lost circulation pressure," in *Proceedings of the SPE Annual Technical Conference and Exhibition*, pp. 43–60, New Orleans, LA, USA, September 1990.
- [3] J. Bruton, C. Ivan, and T. Heinz, "Lost circulation control: evolving techniques and strategies to reduce downhole mud losses," in *Proceedings of the SPE/IADC Drilling Conference*, pp. 1–9, Amsterdam, Netherlands, February 2001.
- [4] Y. Feng and K. E. Gray, "Review of fundamental studies on lost circulation and wellbore strengthening," *Journal of Petroleum Science and Engineering*, vol. 152, pp. 511–522, 2017.
- [5] J. A. A. Oliveira, J. Zago, C. E. Fontes, A. T. A. Waldmann, and A. L. Martins, "Modeling drilling fluid losses in fractured reservoirs," in *Proceedings of the SPE Latin America and Caribbean Petroleum Engineering Conference*, SPE 151021-PP, Mexico City, Mexico, April 2012.
- [6] D. K. Clapper, J. J. Szabo, S. P. Spence et al., "One sack rapid mix and pump solution to severe lost circulation," in *Proceedings of the SPE/IADC Drilling Conference and Exhibition*, SPE/IADC 139817, Amsterdam, Netherlands, March 2011.
- [7] W. W. Sanders, R. N. Williamson, C. D. Ivan, and D. Powell, "Lost circulation assessment and planning program : evolving strategy to control severe losses in deepwater projects," in *Proceedings of the SPE/IADC Drilling Conference*, SPE/IADC 79836, Amsterdam, Netherlands, February 2003.
- [8] G. Wang and X. Pu, "Discrete element simulation of granular lost circulation material plugging a fracture," *Particulate Science and Technology*, vol. 32, no. 2, pp. 112–117, 2014.
- [9] H. Wang, R. Sweatman, B. Engelman, W. D. Halliburton, and D. Whitfill, "The key to successfully applying today's lost circulation solutions," in *Proceedings of the SPE Annual Technical Conference and Exhibition*, SPE 95895, Dallas, TX, USA, October 2005.
- [10] D. Whitfill, "Lost circulation material selection, particle size distribution and fracture modeling with fracture simulation software," in *Proceedings of the IADC/SPE Asia Pacific Drilling Technology Conference and Exhibition*, pp. 1–12, Jakarta, Indonesia, August 2008.
- [11] R. Silva, F. A. P. Garcia, P. M. G. M. Faia, and M. G. Rasteiro, "Settling suspensions flow modelling: a review," *KONA Powder and Particle Journal*, vol. 32, pp. 41–56, 2015.
- [12] Y. Tsuji, T. Kawaguchi, and T. Tanaka, "Discrete particle simulation of two-dimensional fluidized bed," *Powder Technology*, vol. 77, no. 1, pp. 79–87, 1993.
- [13] H. Kruggel-Emden, E. Simsek, S. Rickelt, S. Wirtz, and V. Scherer, "Review and extension of normal force models for the discrete element method," *Powder Technology*, vol. 171, no. 3, pp. 157–173, 2007.
- [14] Z. G. Luo, H. Zhou, T. Zhang et al., "DEM study of blockage behaviour of cohesive fine particles in a packed structure of large particles," *Powder Technology*, vol. 314, pp. 102–109, 2016.
- [15] S. Al-Arkawazi, C. Marie, K. Benhabib, and P. Coorevits, "Modeling the hydrodynamic forces between fluid-granular medium by coupling DEM-CFD," *Chemical Engineering Research and Design*, vol. 117, pp. 439–447, 2017.
- [16] M. Karimi, N. Mostoufi, R. Zarghami, and R. Sotudeh-Gharebagh, "A new method for validation of a CFD-DEM model of gas-solid fluidized bed," *International Journal of Multiphase Flow*, vol. 47, pp. 133–140, 2012.
- [17] A. Esteghamatian, M. Bernard, M. Lance, A. Hammouti, and A. Wachs, "Micro/meso simulation of a fluidized bed in a homogeneous bubbling regime," *International Journal of Multiphase Flow*, vol. 92, pp. 93–111, 2017.
- [18] R. Sun and H. Xiao, "Diffusion-based coarse graining in hybrid continuum-discrete solvers: theoretical formulation and a priori tests," *International Journal of Multiphase Flow*, vol. 77, pp. 142–157, 2015.
- [19] N. G. Deen, M. Van Sint Annaland, M. A. Van der Hoef, and J. A. M. Kuipers, "Review of discrete particle modeling of fluidized beds," *Chemical Engineering Science*, vol. 62, no. 1-2, pp. 28–44, 2007.
- [20] L. A. Ni, A. B. Yu, G. Q. Lu, and T. Howes, "Simulation of the cake formation and growth in cake filtration," *Minerals Engineering*, vol. 19, no. 10, pp. 1084–1097, 2006.
- [21] F. Qian, N. Huang, J. Lu, and Y. Han, "CFD-DEM simulation of the filtration performance for fibrous media based on the mimic structure," *Computers & Chemical Engineering*, vol. 71, pp. 478–488, 2014.
- [22] F. Qian, N. Huang, X. Zhu, and J. Lu, "Numerical study of the gas-solid flow characteristic of fibrous media based on SEM using CFD-DEM," *Powder Technology*, vol. 249, pp. 63–70, 2013.
- [23] W. Li, S. Shen, and H. Li, "Study and optimization of the filtration performance of multi-fiber filter," *Advanced Powder Technology*, vol. 27, no. 2, pp. 638–645, 2016.
- [24] K. J. Dong, R. P. Zou, R. Y. Yang, A. B. Yu, and G. Roach, "DEM simulation of cake formation in sedimentation and filtration," *Minerals Engineering*, vol. 22, no. 11, pp. 921–930, 2009.
- [25] S. Akhshik, M. Behzad, and M. Rajabi, "CFD-DEM simulation of the hole cleaning process in a deviated well drilling: the effects of particle shape," *Particology*, vol. 25, pp. 72–82, 2016.
- [26] S. Akhshik, M. Behzad, and M. Rajabi, "CFD-DEM approach to investigate the effect of drill pipe rotation on cuttings transport behavior," *Journal of Petroleum Science and Engineering*, vol. 127, pp. 229–244, 2015.
- [27] S. Akhshik and M. Rajabi, "CFD-DEM modeling of cuttings transport in underbalanced drilling considering aerated mud effects and downhole conditions," *Journal of Petroleum Science and Engineering*, vol. 160, pp. 229–246, 2018.
- [28] B. Pang, S. Wang, Q. Wang et al., "Numerical prediction of cuttings transport behavior in well drilling using kinetic theory of granular flow," *Journal of Petroleum Science and Engineering*, vol. 161, pp. 190–203, 2018.
- [29] J. Chen, K. Chu, R. Zou et al., "Systematic study of the effect of particle density distribution on the flow and performance of a dense medium cyclone," *Powder Technology*, vol. 314, pp. 510–523, 2016.
- [30] X. Ku, J. Lin, M. van Sint Annaland, and R. Hagemeijer, "Numerical simulation of the accumulation of heavy particles in a circular bounded vortex flow," *International Journal of Multiphase Flow*, vol. 87, pp. 80–89, 2016.
- [31] Z. Y. Yu, C. L. Wu, A. S. Berrouk, and K. Nandakumar, "Discrete particle modeling of granular Rayleigh-Taylor

- instability,” *International Journal of Multiphase Flow*, vol. 77, pp. 260–270, 2015.
- [32] A. G. Kidanemariam and M. Uhlmann, “Interface-resolved direct numerical simulation of the erosion of a sediment bed sheared by laminar channel flow,” *International Journal of Multiphase Flow*, vol. 67, pp. 174–188, 2014.
- [33] G. Mallouppas and B. van Wachem, “Large eddy simulations of turbulent particle-laden channel flow,” *International Journal of Multiphase Flow*, vol. 54, pp. 65–75, 2013.
- [34] Y. Guo and X. Yu, “Comparison of the implementation of three common types of coupled CFD-DEM model for simulating soil surface erosion,” *International Journal of Multiphase Flow*, vol. 91, pp. 89–100, 2017.
- [35] A. Volk, U. Ghia, and C. Stoltz, “Effect of grid type and refinement method on CFD-DEM solution trend with grid size,” *Powder Technology*, vol. 311, pp. 137–146, 2017.
- [36] M. Robinson and M. Ramaioli, “Mesoscale fluid-particle interaction using two-way coupled SPH and the Discrete Element Method,” in *Proceedings of the 6th International SPHERIC Workshop*, Hamburg, Germany, June 2011.
- [37] K. Washino, E. L. Chan, K. Miyazaki, T. Tsuji, and T. Tanaka, “Time step criteria in DEM simulation of wet particles in viscosity dominant systems,” *Powder Technology*, vol. 302, pp. 100–107, 2016.
- [38] H. P. Zhu, Z. Y. Zhou, R. Y. Yang, and A. B. Yu, “Discrete particle simulation of particulate systems: theoretical developments,” *Chemical Engineering Science*, vol. 62, no. 13, pp. 3378–3396, 2007.
- [39] W. Zhong, A. Yu, X. Liu, Z. Tong, and H. Zhang, “DEM/CFD-DEM modelling of non-spherical particulate systems: theoretical developments and applications,” *Powder Technology*, vol. 302, pp. 108–152, 2016.
- [40] V. Dokhani, Y. Ma, and M. Yu, “Determination of equivalent circulating density of drilling fluids in deepwater drilling,” *Journal of Natural Gas Science and Engineering*, vol. 34, pp. 1096–1105, 2016.
- [41] M. Zamora, P. N. Broussard, and M. P. Stephens, “The top 10 mud-related concerns in deepwater drilling operations,” in *Proceedings of the SPE International Petroleum Conference and Exhibition in Mexico*, Villahermosa, Mexico, February 2000.
- [42] R. Caenn and G. V. Chillingar, “Drilling fluids: state of the art,” *Journal of Petroleum Science and Engineering*, vol. 14, no. 3–4, pp. 221–230, 1996.
- [43] M. R. P. Tingay, J. Reinecker, and B. Müller, “Borehole breakout and drilling-induced fracture analysis from image logs,” *World Stress Map Project Guidelines: Image Logs*, 2008.
- [44] M. Brudy and M. D. Zoback, “Drilling-induced tensile wall-fractures: implications for determination of in-situ stress orientation and magnitude,” *International Journal of Rock Mechanics and Mining Sciences*, vol. 36, no. 2, pp. 191–215, 1999.
- [45] Z. Zhang and Q. Chen, “Comparison of the Eulerian and Lagrangian methods for predicting particle transport in enclosed spaces,” *Atmospheric Environment*, vol. 41, no. 25, pp. 5236–5248, 2007.
- [46] G. Gouesbet and a. Berlemont, “Eulerian and Lagrangian approaches for predicting the behaviour of discrete particles in turbulent flows,” *Progress in Energy and Combustion Science*, vol. 25, no. 2, pp. 133–159, 1998.
- [47] B. Popoff and M. Braun, “A Lagrangian approach to dense particulate flows,” in *Proceedings of the ICMF 2007 6th International Conference on Multiphase Flow*, p. 11, Leipzig, Germany, July 2007.
- [48] S. Elghobashi, “On predicting particle-laden turbulent flows,” *Applied Scientific Research*, vol. 52, no. 4, pp. 309–329, 1994.
- [49] P. A. Cundall and O. D. L. Strack, “A discrete numerical model for granular assemblies,” *Géotechnique*, vol. 29, no. 1, pp. 47–65, 1979.
- [50] S. A. Morsi and A. J. Alexander, “An investigation of particle trajectories in two-phase flow systems,” *Journal of Fluid Mechanics*, vol. 55, no. 2, p. 193, 1972.
- [51] A. Li and G. Ahmadi, “Dispersion and deposition of spherical particles from point sources in a turbulent channel flow,” *Aerosol Science and Technology*, vol. 16, no. 4, pp. 209–226, 1992.
- [52] A. A. Kendoush, A. H. Sulaymon, and S. A. M. Mohammed, “Experimental evaluation of the virtual mass of two solid spheres accelerating in fluids,” *Experimental Thermal and Fluid Science*, vol. 31, no. 7, pp. 813–823, 2007.
- [53] S. Luding, “Collisions & contacts between two particles,” in *Physics of Dry Granular Media*, H. J. Herrmann, J.-P. Hovi, and S. Luding, Eds., Springer, Dordrecht, Netherlands, pp. 285–304, 1998.
- [54] G. Kuwabara and K. Kono, “Restitution coefficient in a collision between two spheres,” *Japanese Journal of Applied Physics*, vol. 26, no. 8, pp. 1230–1233, 1987.
- [55] A. Hager, C. Kloss, S. Pirker, and C. Goniva, “Parallel resolved open source CFD-DEM: method, validation and application,” *The Journal of Computational Multiphase Flows*, vol. 6, no. 1, pp. 13–27, 2014.
- [56] S. Ma, Z. Wei, and X. Chen, “CFD-DEM combined the fictitious domain method with Monte Carlo method for studying particle sediment in fluid,” *Particulate Science and Technology*, vol. 36, no. 8, pp. 920–933, 2018.
- [57] G. Pozzetti, H. Jasak, X. Besseron, A. Rousset, and B. Peters, “A parallel dual-grid multiscale approach to CFD-DEM couplings,” *Journal of Computational Physics*, vol. 378, pp. 708–722, 2019.
- [58] B. Vowinckel, J. Withers, P. Luzzatto-Fegiz, and E. Meiburg, “Settling of cohesive sediment: particle-resolved simulations,” *Journal of Fluid Mechanics*, vol. 858, pp. 5–44, 2019.
- [59] Z. Wang, Y. Teng, and M. Liu, “A semi-resolved CFD-DEM approach for particulate flows with kernel based approximation and Hilbert curve based searching strategy,” *Journal of Computational Physics*, vol. 384, pp. 151–169, 2019.
- [60] Y. Wang, L. Zhou, and Q. Yang, “Hydro-mechanical analysis of calcareous sand with a new shape-dependent fluid-particle drag model integrated into CFD-DEM coupling program,” *Powder Technology*, vol. 344, pp. 108–120, 2019.
- [61] N. Mordant and J.-F. Pinton, “Velocity measurement of a settling sphere,” *The European Physical Journal B*, vol. 18, no. 2, pp. 343–352, 2000.
- [62] P. Gondret, M. Lance, and L. Petit, “Bouncing motion of spherical particles in fluids,” *Physics of Fluids*, vol. 14, no. 2, pp. 643–652, 2002.

Copyright © 2019 Marcos V. Barbosa et al. This is an open access article distributed under the Creative Commons Attribution License (the “License”), which permits unrestricted use, distribution, and reproduction in any medium, provided the original work is properly cited. Notwithstanding the ProQuest Terms and Conditions, you may use this content in accordance with the terms of the License. <http://creativecommons.org/licenses/by/4.0/>